Dislocation glide and dynamic recrystallization in LiF single crystals

O. Sitdikov *, R. Kaibyshev

Abstract

Single crystals of LiF with ⟨111⟩ orientation have been dynamically recrystallized during steady state of plastic deformation at 673 K. It is shown that localization of single dislocation glide plays an important role in the initiation of continuous dynamic recrystallization. Bands of elongated subgrains of rectangular shape are formed in areas of localized deformation at small strains. Upon subsequent deformation uniform multiple slip occurs and leads to the formation of equiaxed subgrains between bands of elongated subgrains. Further plastic deformation leads to a continuous increase in misorientation of subgrain boundaries and their eventual conversion into high angle boundaries. The mechanisms of the formation of recrystallized grains with different grain boundary configurations and the relationship between grain boundary configuration and character of dislocation slip are discussed.

1. Introduction

The main mechanism of grain boundary formation during plastic deformation in materials with a high value of stacking-fault energy (SFE) is gradual conversion of low angle grain boundaries into high angle ones [1–8] through a continuous dynamic recrystallization (CDRX) mechanism. This type of structure evolution has often been observed in minerals (olivine [2], sodium and potassium chlorides [3,4]) and metals (pure aluminum [5], aluminum and β-titanium [1,6,7] alloys and ferritic steels [8]). However, although the experimental observations of structural evolution in these works were quite detailed, some important aspects of CDRX mechanism are unclear. It is well known [1], that the existence of a stable subgrain structure is a main condition for occurrence of CDRX. The interaction between sliding dislocations and a stable low-angle boundary can result in growth of its misorientation and gradual conversion into a high-angle boundary. It was assumed [1] that the stability of subgrain and grain structure in multiphase materials was mainly caused by pinning of boundaries by second-phase particles. However, this assumption is unable to explain the fact of CDRX occurrence in single-phase materials, such as NaCl [3,4] or pure Al [5]. From this point of view, it is interesting to consider the microstructural evolution of a pure high SFE material in detail. LiF is a classical material with high value of SFE. Plastic deformation of LiF single crystals was extensively studied in the past. However, no dynamic recrystallization behavior was reported.

Relationships between deformation mechanisms and processes of CDRX are poorly known. It has been shown [3] that a certain character of dislocation glide effected a certain shape of subgrains. Consequently, it can be expected, that configuration of recrystallized grain boundaries formed during further deformation may be inherited from and, as a result, can be related to the operating deformation mechanism.

Thus, the main aim of the present study is to report occurrence of CDRX in ⟨111⟩-oriented LiF single crystal. In addition, the role of dislocation slip in the formation of the steady state subgrain structure and the mechanism of CDRX will be considered.

2. Materials and experimental technique

Lithium fluoride single crystals (less than 4 ppm divalent impurities) purchased from LOMO Ltd. (Sankt-Peterburg, Russia) were used for our investigations. Crystals to be deformed under applied stress parallel to ⟨111⟩ (Fig. 1a and b) were cut out from cubes of ⟨100⟩-oriented crystals using a wire saw. Samples for tests had the shape of a rectangular parallelepiped being normally 8 mm long and 5 mm thick. The side faces of these samples coincided with {121} and {101} planes of the LiF single crystal. The orientation of axes and faces was tested by X-ray technique. The maximal inaccuracy was 0.5°. The samples were annealed at 873 K for 4–5 h and cooled in the furnace. Finally, the samples were chemically polished.

For microstructural examinations, the compression tests were conducted by use an universal testing machine 'Schenck RMS-1000M' at an initial strain rate of $\dot{\varepsilon} = 4.2 \times 10^{-3}$ s^{-1}, at a temperature of 673 K. The tests were ended by unloading the samples, which were cooled in air.

The true stress σ was determined as a force per current average cross section calculated by assuming constancy of volume and neglecting any barreling that may have occurred. The true compressive strain, ε, was calculated as

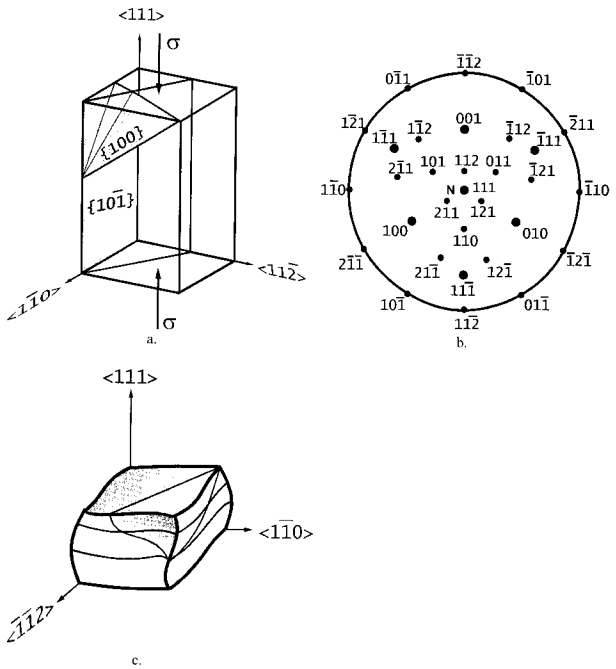

Fig. 1. (a) Sketch of initial specimen. The arrangement of main crystallographic directions and slip planes in specimen is indicated. (b) Positions of the compression axis (N) and main crystallographic directions in the (111) stereographic standard projection of the cubic symmetry crystal. (c) Sketch of specimen deformed up to $\varepsilon = 0.7$.

$$\varepsilon = \ln\left(\frac{h_0}{h}\right) \tag{1}$$

where h and h_0 are the current and the initial height of the sample, respectively. The values of strain hardening rate Θ were estimated as [9]:

$$\Theta = \frac{1}{4}\left(\frac{d\sigma}{d\varepsilon}\right) \tag{2}$$

For microstructural examination, the samples were cut by a wire saw, chemically polished and etched in 30% aqueous solution of fluoboric acid. For purpose of quantitative certification of structure elements revealed by etching a specimen strained up to $\varepsilon = 0.36$ was cut, etched and subjected by repetitive deformation with a true strain of about 0.1. The surface dislocation features were analyzed in conjunction with etched structure. Intersection angles of dislocation features in neighbor grains were used to evaluate misorientation of deformation induced boundaries. The surface relief and the microstructure were studied with the scanning electron microscope JSM-840 and the optical microscopes 'Metaval' and 'Neophot-32'. The X-ray structural analysis was performed by a photo method with a CROS camera using the X-ray device URS-2.0.

Creep tests were carried out to estimate values of the apparent activation energy for deformation (Q_a) and the stress exponent (n). A number of crystals were tested at a constant temperature (about 673 K) and several different stresses or alternatively deformed under constant stress, σ_0, while the temperature was stepwise increased in a narrow range from 673 to 703 K. To ensure that constant stress, σ_0, was maintained throughout the test, additional predetermined load increments were added at engineering strain intervals 0.03 to compensate for the increase in cross-section with compressive strain. Initially, these increments were calculated by assuming constancy of volume. The deformation behavior of the material was analyzed only in the steady state of plastic deformation. In this case, there is no difference between deformation at constant $\dot{\varepsilon}$ and at constant σ_0 [3].

The shear modulus was taken from [10] as:

$$G = 45.8\left[1 - \frac{0.8(T - 300\ \text{K})}{T_m}\right]\ \text{GPa} \tag{3}$$

where $T_m = 1140$ K is the melting point of LiF.

3. Results

3.1. Mechanical testing

A true stress-strain curve of the LiF single crystal for $T = 673$ K and $\dot{\varepsilon} = 4.2 \times 10^{-3}$ s^{-1} is shown in Fig. 2. Four stages of plastic deformation can be denoted. These stages are distinguished by the strain-hardening

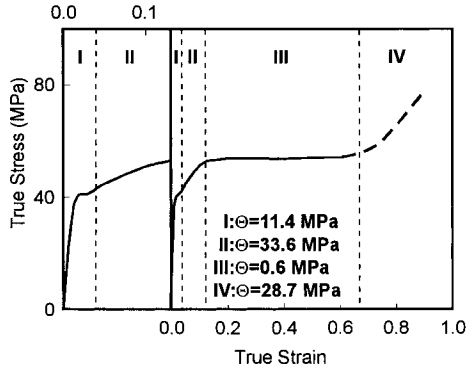

Fig. 2. Stress–strain curve of LiF at $T = 673$ K, $\dot{\varepsilon} = 4.2 \times 10^{-3}$ s^{-1} and strain hardening rate Θ in different strain ranges.

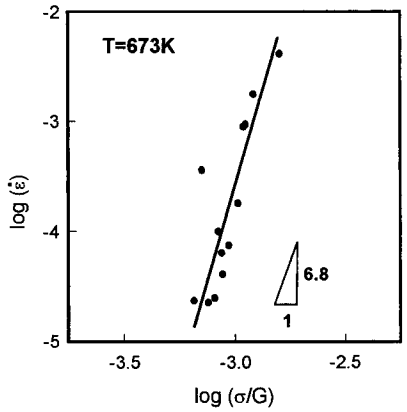

Fig. 3. Strain rate versus normalized stress for ⟨111⟩ oriented LiF single crystals in 'incremental' strain rate test.

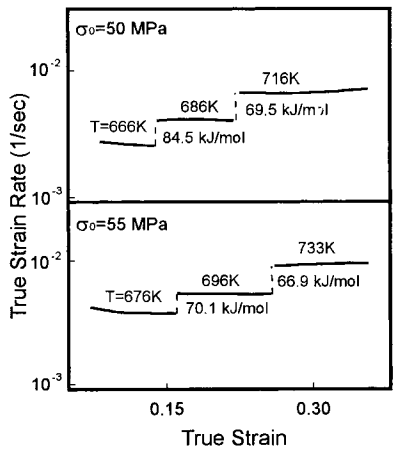

Fig. 4. Strain rate versus strain for ⟨111⟩ oriented LiF single crystals in 'incremental' temperature test.

rate, Θ. The first stage is very short. There is an extensive material hardening in stage II with $\Theta = 33.6$ MPa. The minimal strain hardening rate of 0.6 MPa is observed in stage III. This stage is attained at $\varepsilon = 0.12$. An apparent hardening, which can be caused by influence of friction, with $\Theta = 29$ MPa is observed at $\varepsilon >$ 0.7. Therefore, the third stage is in fact the steady state of deformation. The shape of σ–ε curve presented in Fig. 2 is essentially similar to that of LiF single crystals strained along the ⟨100⟩ axis at similar temperature and strain rate [9,11]. However, in comparison with ⟨100⟩ oriented LiF single crystals, the ⟨111⟩ oriented crystal exhibits higher flow stress, stage I is shorter, and stage III is more extended. Notably, the steady state stress (55 MPa, 4×10^{-3} s^{-1}) fits with high accuracy to the linear dependence of steady state strain rate, log $\dot{\varepsilon}$, against steady state stress, log σ, on a double logarithmic scale obtained by Biberger and Blum [12] for ⟨100⟩ oriented pure LiF single crystals at $T = 673$ K.

The typical specimen compressed up to true strain of about 0.7 is presented in Fig. 1c. It is seen that there exists no remarkable barreling, that may be expected in compression at high strain. A slight bending of two opposite sides of parallelepiped-specimen takes place (Fig. 1c). This bending exhibits a complex shape, which can be interpreted as a result of glide of screw and edge dislocations. Thus, the plastic deformation of ⟨111⟩ LiF single crystals is not uniform at the macroscopic level.

The results of 'incremental' temperature and stress creep tests are presented in Fig. 3 and Fig. 4. It is seen from Fig. 3 that the deformation behavior of ⟨111⟩ oriented LiF single crystals at 673 K obeys by the power law [3,12,13]:

$$\dot{\varepsilon} = A\left(\frac{\sigma}{G}\right)^{n} \exp\left(\frac{-Q_a}{RT}\right), \tag{4}$$

where A is a constant, G is the Shear modulus, R is the universal gas constant per mole, T is the temperature, n is the stress exponent being equal to 6.8.

The average value of $Q_a (\approx R \ln(\dot{\varepsilon}_1/\dot{\varepsilon}_2)/(1/T_2 - 1/T_1))$ [3,13]) calculated for each temperature jump was about 72 kJ mol^{-1} (Fig. 4). This value of Q_a is in good agreement with the data obtained for ⟨100⟩-oriented LiF crystals strained at similar temperature-strain rate conditions [11]. It supports the assumption of invariance of apparent activation energy with crystal orientation [13]. The experimental value of stress exponent ($n = 6.8$) found in the present study is considerably higher than that reported in [11] for ⟨100⟩ oriented LiF single crystals ($n = 3.9$). At the same time it is in agreement with the results ($n = 6.6$) obtained both in [14] for polycrystalline LiF and in [12,15] for ⟨100⟩ oriented pure LiF single crystals.

3.2. Surface observations

The metallographic surface features were found to be dependent on strain. At the end of stage I ('easy-glide' region of plastic flow in the fcc metals [16]) two operating cubic {100} ⟨110⟩ slip systems were observed (Fig. 5a). One of them is dominant. The long straight lines of

this dominant system intersect the body of a single crystal. Their distribution is considerably inhomogeneous.

At stage II, the slip lines cluster in slip line bands (Fig. 5b) that are parallel to the trace of a cubic plane (Fig. 1a). Local shears develop in the material. This results in a remarkable bending of the slip lines by an angle of about 10°. Concurrently, extensive multiple slip begins to occur within slip bands. Slip features belonging to the second cubic system and non-cubic systems were observed on the sample surface.

No dominant cubic system was observed at the onset of stage III (Fig. 5c). The body of the initial LiF single crystal is subdivided into two areas differing by the character of dislocation slip. The first area was defined as bands of slip features belonging to one cubic system. Evidences for secondary slip system operation can be found in some bands. Uniform multiple slip occurs in the second area. Slip features from two or three cubic slip systems were observed in almost all the second areas. These slip features consist of straight and wavy slip lines. The latter is attributed to the occurrence of cross-slip. The cross-slip plane is a {110} plane. In addition, there is an evidence for non-cubic slip operating in separate slip areas (Fig. 5c). Notably the slip features of {110} ⟨110⟩ system deviate from compression axis direction by an angle ranging from 5 to 7°. It is indicative of distortion of crystallite lattice in the second areas.

Further deformation results in an increase in slip homogeneity at stage III. Cross-slip features were found in most areas of the strained sample. Three independent slip systems start to operate (Fig. 5d). A network of slip features belonging to {100} ⟨110⟩ and {110} ⟨110⟩ systems is formed.

3.3. Microstructure evolution

Fig. 6 represents etched {211} surfaces of LiF single crystals strained up to strains, which are associated with the steady state. It is seen that plastic deformation yields the formation of two different structural components. Structural bands with a width of about 10 μm are formed at stage II of plastic flow (Fig. 6a). These bands are non-uniformly arranged along one cubic plane in the LiF single crystal. This is the first component of the microstructure. Note that there is a dominant direction of bands in samples, and that bands parallel to other cubic planes are rarely observed. Etch pits of high density are resolved inside the bands. After etching the longitudinal band boundaries could be recognized as long thick lines. Numerous thin boundaries located in the transverse direction were revealed inside the bands. The transverse boundaries subdivide the bands into separate structural elements. Therefore, the bands comprise arrays of low angle boundaries. Subgrains have a rectangular shape with an aspect ratio of more than 3–4. Separate low angle boundaries were observed in the areas located between the bands. No arrays of deformation induced boundaries was found. These areas constitute the second structural component.

A strain increase leads to the formation of a stable (sub)grain structure within areas of the first structural components (Fig. 6b). Deformation induced boundaries exhibit increased misorientation. The increase of misorientation is visible by enhanced contrast of etched

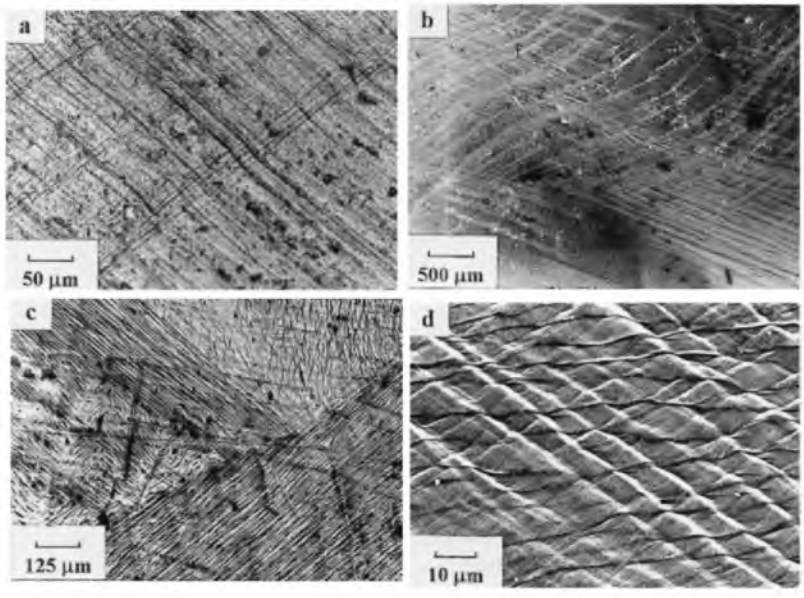

Fig. 5. Deformation relief formed on {211} facet of ⟨111⟩ oriented LiF single crystal during deformation at 673 K and $\dot{\varepsilon} = 4.2 \times 10^{-3}\ s^{-1}$: (a) $\varepsilon = 0.05$; (b) $\varepsilon = 0.09$; (c) $\varepsilon = 0.16$; (d) $\varepsilon = 0.35$.

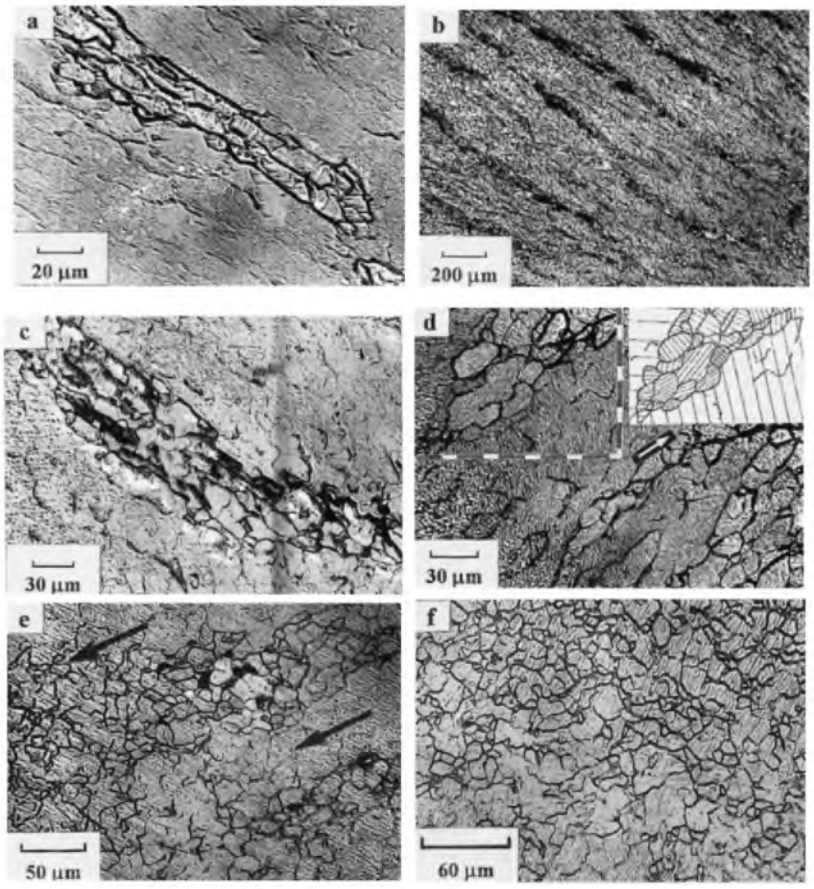

Fig. 6. Microstructure on {211} facet of ⟨111⟩ oriented LiF crystals deformed at 673 K and $\dot{\varepsilon} = 4.2 \times 10^{-3}\ s^{-1}$: (a) $\varepsilon = 0.16$; (b) and (c) $\varepsilon = 0.35$; (d) $\varepsilon = 0.35$ add repetitive strain with $\varepsilon = 0.1$; the insertion in the right top corner of the micrograph is a schematic representation of the structure in the left top corner bounded by dashed lines, the lines in this scheme indicate the directions of active slip plane traces; (e) $\varepsilon = 0.5$; (f) $\varepsilon = 0.7$.

boundaries. Bands with mixed (sub)grain structure are observed in the areas of the first structural component after $\varepsilon = 0.35$ (Fig. 6c). It can be seen that longitudinal and transverse boundaries are mainly high angle and low angle boundaries, respectively. The bands consist of both subgrains and true grains with rectangular shape. These crystallites tend to slightly grow in the transverse direction with increasing strain. Longitudinal low angle boundaries were often observed in the areas of second structural component. Transverse subboundaries are encountered rarely in these areas. It can be concluded that arrays of low angle boundaries begin to form in the second structural component at $\varepsilon = 0.35$.

In order to reveal the origin of deformation induced boundaries, the slip lines formed during additional deformation with a strain of about 0.1 were analyzed in a sample strained up to $\varepsilon = 0.35$ (Fig. 6d). It is seen that the specimen behaves like a polycrystal during additional deformation. Slip features within neighboring crystallites are not parallel each to another, and angles between these slip lines can be used to evaluate misorientation. It is worth noting that no intersection of high angle boundaries by slip lines is observed, and low- and middle-angle boundaries are intersected by slip lines, which deviate at a small angle. Judging the misorientation of slip lines one can conclude that the bands of the first structural component consist of mixed (sub)grain structure. The fraction of longitudinal boundaries in this structure is middle- to high-angle ones. Transverse subboundaries within these bands are mainly characterized by low angle misorientation (Fig. 6d). The bending of slip lines within some elongated (sub)grains indicates a continuous lattice misorientation in bands. Thus, as a rule, the structure elements formed in the bands at strains of about 0.35–0.40 are bounded by pair of high-angle longitudinal and pair of low-angle transverse boundaries (Fig. 6c and d). Misorientation of boundaries of the second structural component is low angle misorientation. Therefore, boundaries of the first structural component can exhibit high angle misorientation, and boundaries located in areas between bands of elongated grains exhibit low angle misorientation only.

The fraction of high-angle boundaries increases and equiaxed grains are formed within the bands with increasing strain (Fig. 6e). The average size of grains and subgrains is almost similar here. In addition, a well-

defined (sub)grain structure is formed with increasing strain in the areas between the bands of recrystallized structure. Separate low angle boundaries are rarely observed here at $\varepsilon = 0.5$. The formation of transverse boundaries in the second structural component provides the formation of crystallites surrounded by boundaries from all sides. As a result, arrays of deformation induced boundaries highly dominates in the second structural component after $\varepsilon = 0.5$. Most of these boundaries are high angle boundaries (arrows in the Fig. 6e indicate these areas). Note that the formation of equaixed subgrains and their evolution into a recrystallized structure is observed at lower strain in the former band structure in comparison with the second structural component.

Further deformation results in the formation of a uniform recrystallized structure consisting of equiaxed grains. It is impossible to reveal a dominant orientation of grain boundaries in respect to different crystallographic directions (Fig. 6f). The triple junction angles of these grains tend to 120°. The average grain size is ranging from 10 to 15 μm. After $\varepsilon = 0.7$, the volume fraction of the recrystallized structure is about 80% and the recrystallized grains occupy the whole material volume after a true strain of 1. No significant changes of recrystallized structure were revealed at true strains ranging from 0.7 to 1.

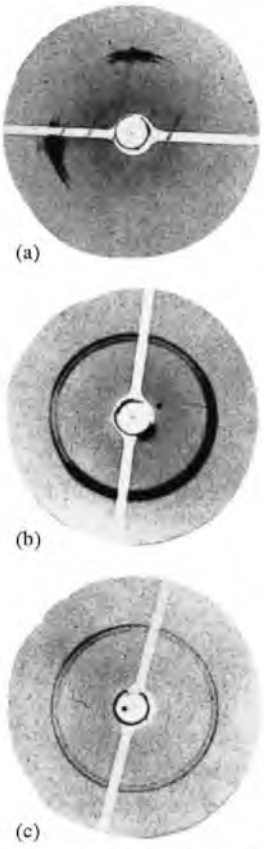

Fig. 7. Diffraction patterns on {111} facet of ⟨111⟩ oriented LiF crystals deformed at 673 K and $\dot{\varepsilon} = 4.2 \times 10^{-3}\ s^{-1}$: (a) $\varepsilon = 0.15$; (b) $\varepsilon = 0.35$; (c) $\varepsilon = 0.7$.

3.4. X-ray analysis

Data from the photo method support the results of microstructural observations. At stage II, the diffraction spots are diffused and tend to elongate toward azimuthal direction by 1–5° (Fig. 7a). Diffraction spots tend to form ring. These elongated spots are indicative of bending of crystal lattice. At a true strain of 0.35, the diffraction spots are highly diffuse and form rings (Fig. 7b). There is evidence for the formation of subgrains and first recrystallized grains occurring at the onset of the stage III. At strains ranging from 0.35 to 0.5, a strong crystallographic texture associated with the initial single crystal orientation was revealed in the former single crystals. Numerous spots randomly arranged in rings were observed in diffraction patterns after $\varepsilon = 0.7$ (Fig. 7c). These spots are only slightly diffuse. Thus, the diffraction pattern shows that the deformation induced grain boundaries have high angles of misorientation. At the end of stage III, a texture randomization is observed (Fig. 7c).

4. Discussion

The results presented show that CDRX occurs in the LiF single crystals during plastic deformation at a temperature of 673 K. CDRX was observed in numerous materials with high SFE at elevated temperature [17], and the stages of CDRX can be summarized as follows:

(i) stable subgrain structure forms at lower strains;
(ii) part of low-angle boundaries progressively transforms into true high-angle grain boundaries by dislocation accumulation during plastic deformation;
(iii) migration of new grain boundaries occurs at a low rate.

This scheme of grain formation can be used to describe the microstructural evolution in ⟨111⟩-oriented LiF single crystals at the temperature of 673 K. The formation of a well-defined subgrain structure and subsequent conversion of low angle boundaries into true high angle boundaries take place at the steady state of plastic deformation. Therefore, CDRX plays the role of a restoration process. This process can be the specific restoration mechanism in ⟨111⟩-oriented LiF single crystals. It is known [18–20] that in ⟨100⟩ oriented single crystals of LiF at slightly higher temperature of 773 K, an extensive migration of deformation induced subboundaries, which results in annihilation of dislocations, provides restoration. No CDRX has been observed in ⟨100⟩ oriented single crystals of LiF at $T = 773$ and 923 K [18–20]. Recrystallization behavior of ⟨111⟩-oriented LiF single crystals can be caused by the formation of stable subgrain boundary arrays. It is known that the CRDX strongly depend on the crystal-

Table 1
Values of S_{max} for various slip planes and orientations of compression axes (in brackets, number of equivalent slip systems) [22]

Slip plane	Orientation of axis of compression		
	[001]	[111]	[110]
{110}	0.50 (4)	0.00 (0)	0.25 (4)
{100}	0.00 (0)	0.46 (3)	0.35 (4)
{111}	0.20 (8)	0.27 (6)	0.20 (4)

lographic orientation [17]. Therefore, as initial orientation strongly effects dislocation glide in LiF single crystals, the recrystallization behavior of ⟨111⟩-oriented LiF single crystals can be associated with features of dislocation slip. Thus DRX in these LiF single crystals are affected by the operating deformation mechanism as in metallic materials [21].

4.1. Analysis of deformation behavior

Careful inspection of the deformation behavior of ⟨111⟩ oriented LiF single crystal has shown that the value of the apparent activation energy for plastic deformation was in good agreement with the value of activation energy for cation vacancy migration in LiF ($Q_{Li^+} = 63$–69 kJ mol^{-1} [13]). The value of $Q_a = 72$ kJ mol^{-1} can be interpreted in terms of high temperature dislocation climb, as a controlling process for plastic deformation [3,13]. However, a value of Q_a (72 kJ mol^{-1}) is considerably less than activation energy for migration of slower-moving anions ($Q_{F^-} = 214$ kJ mol^{-1} [10]). This is not typical for high temperature creep of ionic crystals [3,10]. In addition, the stress exponent, $n \sim 7$ is not in consistent with high temperature climb. It is seen that deformation behavior of ⟨111⟩ oriented LiF single crystal is very complicated and there is an unambiguity in its interpretation. It is possible to presume that the temperature of 673 K ($\approx 0.6\ T_m$, where T_m is the melting point) at strain rate 4.2×10^{-3} s^{-1} lies in the range of warm deformation for the single crystal as for metallic materials [10]. i.e. the low temperature dislocation climb can take place. This type of dislocation climb is controlled by vacancy diffusion along dislocation cores and may cause dislocation rearrangement at small distances. In addition, it can be concluded from surface observations that cross-slip plays an important role in dislocation rearrangements. The results obtained indicate that the dynamic recovery occurring at temperature of 673 K is not so extensive to reduce significantly the dislocation density stored during deformation. Therefore, the steady state flow stress could be associated with occurrence of CDRX.

4.2. Slip systems

Two different types of recrystallized structure distinguished by the configuration of grain boundaries and formed at the steady state can be attributed to two types of dislocation glide operating in ⟨111⟩ oriented LiF single crystals. It is known [16,22], that no {110} ⟨110⟩ slip systems can operate in a ⟨111⟩-oriented single crystal of cubic symmetry due to the fact that their Schmid factor, S, is equal to zero (Table 1). For this single crystal orientation, three cube planes {100} are most favorable for slip (Table 1 Fig. 1b). However, it was found for materials having the sodium chloride structure that a {110} ⟨110⟩ system can be operative at an insignificant (less than 3–5°) deviation of the of crystal axis from the given ⟨111⟩ orientation [22]. This is caused by the fact that there is a large difference between values of the critical shear stresses (τ_0) for dislocation slip on {100} and {110} planes. The ratios τ/τ_0 for primary {100} ⟨110⟩ and secondary {110} ⟨110⟩ slip systems, where τ is the shear stress in a slip plane, become comparable even at $S_{(110)} < 0.2S_{(100)}$ for NaCl [22] and at $S_{(110)} < 0.1S_{(100)}$ for LiF [9].

Therefore, in the ⟨111⟩-oriented LiF single crystals the operation of the {100} ⟨110⟩-systems is dominant only at small strains. The dominant slip is localized at mesoscopic level in the form of slip line bands. Development of localized deformation leads to the formation of dislocation pile-ups and a strong bending of the crystal lattice (Fig. 8). The gradual lattice rotation facilitates the operation of the {110} ⟨110⟩ slip systems, and, as a result, non-cubic slip of dislocations with Burgers vector $\boldsymbol{b}_3$ (Fig. 8) and cross-slip become operative. This results in the interaction between dislocations belonging to various slip systems and the strong strain hardening at the second stage of plastic deformation [22].

4.3. CDRX

Onset of CDRX results in the establishment of steady state of plastic flow at which a dynamic equilibrium between hardening by dislocation storage and softening by recrystallization takes place. As it was mentioned above, an extensive collision of deformation induced low angle boundaries of opposite sign leads to their complete dissolution in ⟨100⟩ LiF single crystals [18] in which the steady state is associated with mutual dislocation annihilation. This process does not occur in ⟨111⟩ LiF single crystals, in which the localization of dislocation slip in one cubic plane results in the formation of highly stable low angle boundaries. In the regions of localized deformation, the forming pile-ups of lattice dislocations belonging to {100} ⟨110⟩ system play a role of barriers for mobile dislocations of other systems (Fig. 8). As a result, an extensive accumulation

of dislocations with different Burgers vectors takes place here (Fig. 8). Following dislocation, rearrangements by cross-slip or climb yields the formation of longitudinal subboundaries consisting of twist and tilt components (Fig. 9a). Such low angle boundaries are characterized by low mobility [23] and have non-compensated long-range stress fields [24]. The formation of such subboundaries initiates CDRX. Following deformation results in the formation of transverse subboundaries in the areas of localized deformation and low angle boundaries in areas of uniform deformation (Fig. 9a). Long-range non-compensated stress fields originated from the longitudinal subboundaries interact

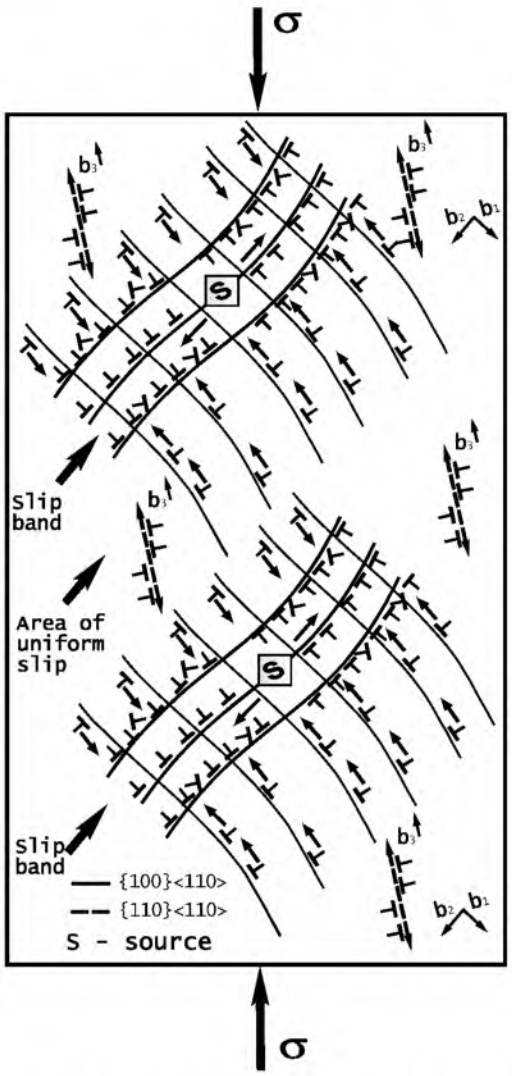

Fig. 8. Schematic drawing of dislocation structure in the slip bands. Accumulation of dislocations of similar sign in slip bands leads to continuous bend of lattice and non-cubic slip systems become operative in ⟨111⟩ oriented LiF single crystals during deformation. The arrows indicate the direction of motion of the individual dislocations emitted by the sources. Pile-ups of dislocation belonging to one cubic system are formed. Dislocations with other Burgers vector accumulate within these pile-ups.

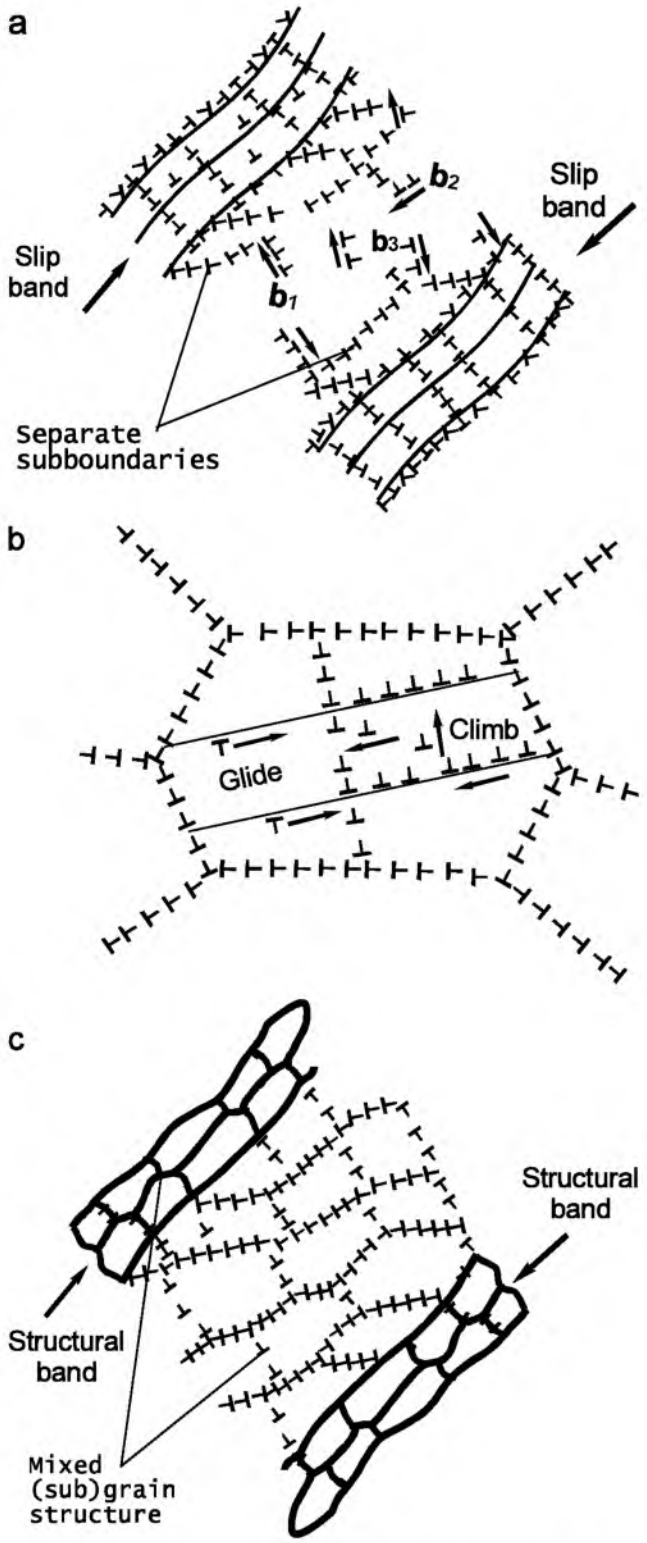

Fig. 9. Schematic representation of structure evolution in ⟨111⟩ oriented LiF single crystals during deformation: (a) the formation of subgrain structure; bands of elongated subgrains alternate with areas of separate low angle boundaries; (b) introduction of mobile lattice dislocations into a low angle boundary; this process provides gradual increment in misorientation; (c) the formation of mixed (sub)grain structure; bands of recrystallized grains alternate with arrays of low angle boundaries.

with short-range stress fields originated from other deformation induced low angle boundaries. This interaction provides high stability of transverse subboundaries and low angle boundaries formed in the areas of uniform deformation. It prevents collision of migrating subboundaries [18] and, as a result, no remarkable coarsening of subgrain structure [25] takes place.

Mobile lattice dislocations intrude into low angle boundaries during subsequent deformation (Fig. 9b). This process results in an increase of dislocation density of subboundaries, and low angle boundaries eventually convert to high angle boundaries. The longitudinal subboundaries containing enhanced dislocation density primarily transform into true high angle boundaries. At further deformation, a gradual increase in the misorientation of the transverse boundaries and the low angle boundaries formed in the areas of uniform deformation leads to their transformation into high angle boundaries too. As a result, the first recrystallized grains form at the sites of former bands of elongated subgrains and inherit their shape (Fig. 9c). In areas of uniform deformation, the equiaxed subgrains gradually evolve into recrystallized grains with strain and the formation of recrystallized grains are detected here at higher strain. Subsequent grain boundary migration provides the formation of an equilibrium network of high-angle boundaries in the site of prior band structure. The new grains formed have the equilibrium shape with angles in triple junctions of about 120°. Despite this fact, no remarkable growth of crystallites takes place.

5. Conclusion

Three stages of plastic deformation distinguished by strain-hardening rate are revealed at the true stress–strain curve of the ⟨111⟩ oriented LiF single crystal for $T = 673$ K and $\dot{\varepsilon} = 4.2 \times 10^{-3}\ s^{-1}$. At stages I and II, the localization of {100} ⟨110⟩ dominant single slip takes place at the mesoscopic level in the form of slip line bands. At further deformation, the lattice rotation initiates {110} ⟨110⟩ slip system operation. As a result, uniform multiple slip is operative in stage III.

The stress dependence of the steady-state strain rate for the ⟨111⟩-oriented LiF single crystal at a temperature of 673 K can be described by the power law equation with a value of the stress exponent $n = 6.8$. The activation energy for plastic deformation at a strain rate of $4.2 \times 10^{-3}\ s^{-1}$ was found to be equal to 72 kJ mol^{-1}.

Continuous dynamic recrystallization occurs in the ⟨111⟩-oriented LiF single crystal in steady state at a temperature of 673 K and strain rate of $4.2 \times 10^{-3}\ s^{-1}$. A fully recrystallized structure forms after true strain of 0.7.

Localization of dislocation slip plays an important role in CDRX occurrence. Two different structural components form in material during deformation. In the site of localized deformation, the elongated (sub)grains form and in the site of uniform deformation, the equiaxed (sub)grains form. Plastic deformation results in gradual conversion of subgrains into recrystallized grains.

Acknowledgements

The authors are thankful to Dr N.P. Skvortsova (A.V. Shubnikov Institute of Crystallography, Russian Academy of Sciences, Moscow) for a very helpful discussion of the results of this work. The support of this research by the Russian Federal Program "Integratsiya" under Grant N A0004 is gratefully acknowledged.

References

[1] S.J. Hales, T.R. McNelley, Acta Metall. 36 (1988) 1229.
[2] J.-P. Poirier, A.J. Nicolas, J. Geol. 83 (1975) 707.
[3] J.-P. Poirier, Plasticite a Haute Temperature des Solides Cristallines, Ed. Eyrolies, Paris, 1976, p. 272.
[4] M. Guillope, J.-P. Poirier, J. Geophys. Res. 84 (1979) 5557.
[5] Ch. Perdrix, M.Y. Perrin, F. Montheillet, Mem. Et. Sci. Rev. Metall./CIT 78 (1981) 975.
[6] T. Sakai, H. Yang, H. Miura, Mater. Sci. Eng. A234-236 (1997) 857.
[7] F. Chaussy, J.H. Driver, Rev. Metall. CIT/Sci. Genie. Mat. 93 (1996) 1057.
[8] A. Belyakov, R. Kaibyshev, Phys. Met. Metallogr. 78 (1994) 91.
[9] N.P. Skvortzova, G.V. Berezhkova, Cryst. Res. Technol. 21 (1986) 939.
[10] H.J. Frost, M.F. Ashby, Deformation-Mechanism Maps, Pergamon Press, Oxford, 1982, p. 328.
[11] N.P. Skvortzova, Cryst. Res. Technol. 31 (1996) 373.
[12] M. Biberger, W. Blum, Scr. Mater. 23 (1989) 1419.
[13] D.R. Groper, J.A. Pask, Phil. Mag. 27 (1973) 1105.
[14] T.G. Langdon, J.A. Pask, Acta Metall. 18 (1970) 505.
[15] G. Streb, B. Reppich, Phys. Stat. Sol. 16A (1973) 493.
[16] R.W.K. Honeycombe, The Plastic Deformation of Metals, Edward Arnold Publishers Ltd, 1968, p. 408.
[17] S. Gourdet, F. Montheillet, Mater. Sci. Eng. A263 (2000) 274.
[18] M. Biberger, W. Blum, Phil. Mag. A 65 (1992) 757.
[19] M. Biberger, W. Blum, Phil. Mag. A 66 (1992) 27.
[20] W. Muller, M. Biberger, W. Blum, Phil. Mag. A 66 (1992) 717.
[21] A. Galiyev, R. Kaibyshev, G. Gottstein, Acta Mater. 49 (2001) 1199.
[22] W. Franzbecker, Phys. Stat. Sol. 57 (1973) 545.
[23] M.A. Shtremel, The Strength of Alloys, Part 1, Lattice Defects (in Russian), MISIS, Moscow, 1999, p. 231.
[24] H. Mughrabi, Acta Metall. 31 (1983) 1367.
[25] G. Eggeler, W. Blum, Phil. Mag. A 44 (1981) 1065.